ROLE OF CARAPACE MORPHOLOGY IN DYNAMIC STABILITY OF RIGID-BODIED BOXFISHES

I.K. Bartol, M.S. Gordon
University of California, Los Angeles
Department of Organismic Biology, Ecology, and Evolution, Los Angeles, CA 90095-1606, U.S.A.
Email: ikbartol@lifesci.ucla.edu, msgordon@ucla.edu

M. Gharib
California Institute of Technology
Option of Bioengineering, Pasadena, CA 91125, U.S.A.
Email: mory@caltech.edu

D. Weihs
Technion
Department of Aerospace Engineering, Haifa, 32000, Israel.
Email: dweihs@techunix.technion.ac.il

P. Webb
University of Michigan
School of Natural Resources and Department of Biology, Ann Arbor, MI, 48109, U.S.A.
Email: pwebb@umich.edu

Abstract

The marine boxfishes (Teleostei: Ostraciidae) are noteworthy for their rigid bony carapaces (tests) that encase the forward 2/3-3/4 of their bodies, restricting body movements to their fins and posterior sections of their tails. The bony exteriors of boxfishes are keeled with various protuberances, features that distinguish them from most fishes and manmade autonomous underwater vehicles, which have more rounded perimeters. Given that swimming boxfishes maintain unusually steady course directions with minimal rolling, pitching, and yawing, the goal of our research program is to determine the role of carapace morphology in dynamic stability of swimming boxfishes. For this paper, we focus on one species, the smooth trunkfish *Lactophrys triqueter*, which is triangular in cross section with sharp ventro-lateral keels and no significant ornamentation. Detailed stereolithographic, rapid-prototype models of the carapace were generated from computerized tomographic (CT) scans. The models were positioned at various angles of attack in water or wind tunnels, and flow patterns around each model were investigated using three methods: 1) digital particle image velocimetry (DPIV), 2) local pressure measurements, and 3) integral force measurements. Well-developed vortices formed along the ventro-lateral keels of the smooth trunkfish; circulation within regions of vorticity increased posteriorly and intensified as angles of attack became more positive or negative. At positive angles of attack, vortices developed above ventro-lateral keels along lateral concavities. At negative angles of attack, vortices developed below ventro-lateral keels underneath the carapace. Pressure distribution results were generally consistent with these findings, with areas of low pressure correlating well with attached regions of vorticity. Lift coefficients of smooth trunkfish were similar to lift coefficients in delta wings of similar aspect ratio—structures that also generate lift through vortex generation—with stall not occurring at angles of attack between –30 and +30°. The results of the three independent, but complementary experimental approaches, indicate that the ventro-lateral keels of the smooth trunkfish act as vortex generators, producing overall lift and self-correcting forces for pitching (i.e., the keels generate upward directed forces posterior to the center of mass at positive angles of attack and generate downward directed forces posterior to the center of mass at negative angles of attack). The carapace architecture and keel arrangement of the rigid-bodied smooth trunkfish is therefore relevant for the design of dynamically stable, biomimetic autonomous underwater vehicles.

Introduction

The marine boxfishes (Teleostei: Ostraciidae) are mostly shallow-water, tropical reef-dwelling fishes that have 2/3-3/4 of their body lengths encased in rigid bony carapaces (Nelson, 1994). Consequently, they cannot bend their bodies anterior to their caudal peduncles, and almost all of their swimming movements derive from complex combinations of their five fins. The bony exteriors of the boxfishes are keeled with various protuberances, features that distinguish them from most other fishes and manmade autonomous underwater vehicles, which have rounded perimeters. Field observations and recent studies on the swimming mechanics and physiology of these rigid-bodied, keeled fishes indicate that they are capable of remarkably smooth, energy efficient swimming trajectories, which do not compromise maneuverability (Gordon et al, 2000; Hove et al., 2001). The goal of our research program is to understand the role of carapace morphology in maintaining stability.

Four species of ostraciid fishes varying in cross-sectional and lengthwise shapes, ornamentation, and keel characteristics are currently being studied. In this paper, we focus on one species, the smooth trunkfish *Lactophrys triqueter*. The smooth trunkfish is predominantly triangular in cross section with ventro-lateral keels that become progressively sharper posteriorly (Fig. 1). The smooth trunkfish has lateral and ventral regions of concavity adjacent to the ventro-lateral keels, a prominent eye ridge, and no significant ornamentation (i.e., it has no anterior horns or posterior extensions of the ventro-lateral keels). Using stereolithographic models of the body, three separate but interrelated techniques were applied to study stability in this fish: 1) digital particle image velocimetry (DPIV), where flow structures were visualized and quantified at a series of transverse planes along the carapace; 2) local pressure measurements, where static pressures were measured at various dorsal, ventral, and lateral surface locations; and 3) integral force measurements, where total drag and lift forces acting on the model were determined using a force balance.

Methods

Model Construction

Two models of a 17.0 cm total length (TL) smooth trunkfish were constructed. The smooth trunkfish was frozen after capture and shipped from Puerto Rico to UCLA, where it was stored in a –70 °C freezer until it was prepared for scanning. Preparation protocol involved inserting several wooden dowels (~ 5 cm) into a Styrofoam block (10 x 10 cm) and placing the thawed specimen on the dowels so that the ventral plate was supported.

Scanning was conducted at the UCLA Department of Radiology using a GE CT\i spiral CT scanner. A continuous scan was performed through the entire fish using a 1.0 mm collimation at 120 kVp, 200 mA, and a 1 s rotation time. A 50% overlap was used so that images were reconstructed every 0.5 mm. A total of 340 consecutive, 2-dimensional, cross-sectional

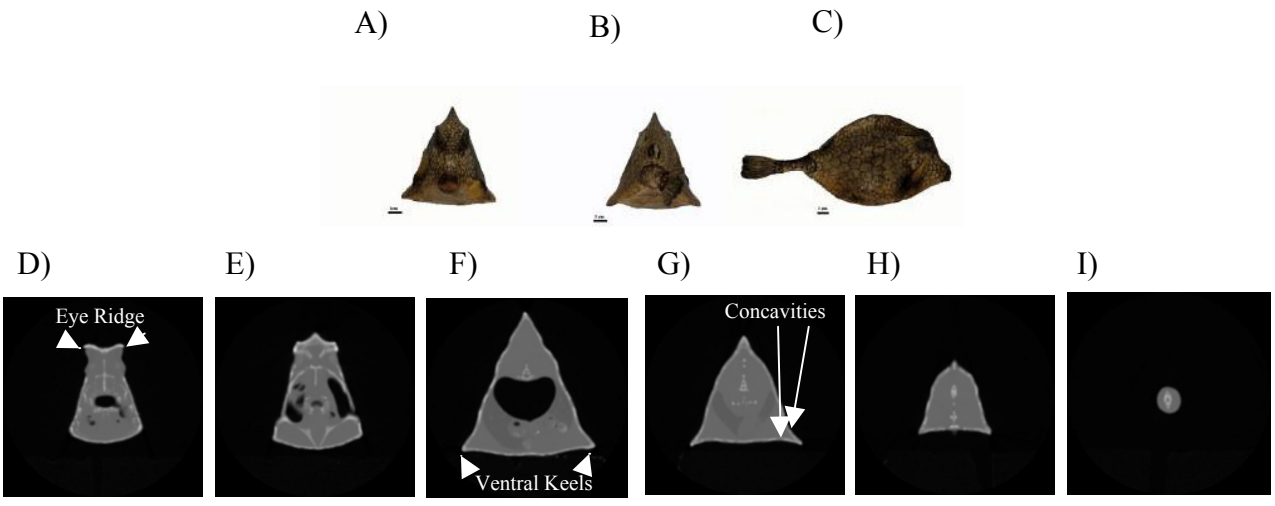

Fig. 1. Anterior, posterior, and lateral views of the smooth trunkfish are depicted in (A), (B), and (C), respectively. The bottom row of images are cross-sectional CT scans of the smooth trunkfish at D) the leading edge of the eye ridge, E) trailing edge of the eye ridge, F) maximum girth, G) midpoint between maximum girth and posterior edge of the carapace, H) posterior edge of the carapace, and I) caudal peduncle.

exposures were generated longitudinally from the snout to tail of the fish. An appropriate threshold (contrast) was selected for maximum resolution, and digital STL models of the fishes were created using a Marching Cubes algorithm, a high-resolution 3D surface construction algorithm (Lorensen and Cline, 1987). Two physical models, one in halves and the other whole, where created from the STL files using stereolithographic rapid-prototyping (Solid Concepts, Inc.) (Fig. 2).

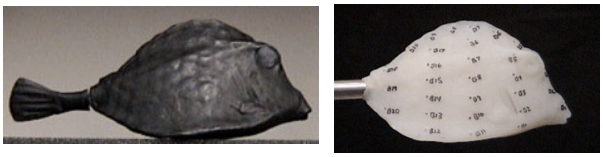

Fig. 2. Models constructed using stereolithographic rapid-prototyping. The model on the left was used in digital particle image velocimetry and force experiments. The model on the right was used in pressure experiments.

Digital Particle Image Velocimetry (DPIV)

A detailed description of the DPIV technique for flow field measurements is provided by Willert and Gharib (1991) and Raffel et al. (1998). Therefore, only a general description of the experimental techniques relevant to this particular experiment is provided below. To reduce glare from laser light, the whole model was painted black. The tail of the model was removed and a 1.0 cm diameter rod (the approximate diameter of the caudal peduncle) was attached to the posterior region of the model. The rod, which was 10 cm in length, was attached to a sting that entered the water tunnel from above. A water tunnel with a 30 x 30 x 100 cm test section (Model 503, Engineering Laboratory Design, Inc., Lake City, MN) seeded with silver-coated hollow glass spheres (14 μm in diameter) was used in the experiment. Two pulsed ND:YAG lasers (wavelength = 532 nm, power rating 50 mJ, [New Wave Research, Fremont, CA]), a series of front-surface mirrors, and a cylindrical lens were used to align and generate an illuminated sheet ~ 1.0 mm thick. The laser sheet was projected underneath the water tunnel in a transverse (YZ) plane. A Pulnix video camera (TM-9701) with a frame size of 460 x 768 pixels and frame rate of 30 Hz was positioned downstream of the working section (unobstructed views of oncoming flow was possible because of a Plexiglas exit tank).

The video camera, lasers, and a Coreco OC-TC10-DIGSE frame grabber (National Instruments, Inc.) were synchronized using a video timing box and *FlowVision*^{TM} software (General Pixels, Pasadena, CA). All experiments were performed in the "master" mode, whereby the video camera generated the timing signals that the frame grabber and lasers locked onto. Generally, the lasers were pulsed for 0.1 ms every 3 ms. The image size used for processing was 480 x 768 pixels, and the interrogation window (i.e., the area over which the particle shifts were averaged) was 32^2 pixels with a 16 pixel offset (50% overlap). The displacement of particles throughout given images over time was calculated by the cross-correlation technique (Willert and Gharib, 1991), and outliers, defined as particle shifts that were 3 or more pixels greater than particles shifts of neighboring particles, were removed and corrected. The data were smoothed to remove high frequency jitter within the video footage and converted from pixels to real units.

DPIV studies were performed around the model as it was positioned at various angles of attack (-30 to +30º) in the water tunnel, which was set at a speed of 2.5 body length s^{-1} (42.5 cm s^{-1}). Flow patterns were examined at five locations along the body of the model: the eye ridge, the point of maximum girth, the midpoint between the point of maximum girth and the posterior edge of the carapace, the posterior edge of the carapace, and the caudal peduncle.

Pressure Measurements

The second smooth trunkfish model, constructed in halves but identical in dimensions to that used in DPIV studies, was used for pressure experiments (Fig. 2). One of the model halves was hollowed out, and 36 holes were drilled in lateral and ventral regions. Urethane tubing (0.068 cm ID, 0.129 cm OD) was inserted into the holes and glued in place so that the tubing was flush with the model surface. The two model halves were glued together. Tubing exited the model through a 1.0 cm rod attached to a posterior section of the model. The rod was used to mount the model in a 61 cm wind tunnel (model 407, Engineering Laboratory Design, Inc., Lake City, MN). The tubing was connected to a Scanivalve 48-channel sampler and a Barocel pressure sensor. Static pressure (N m^{-2}) at each of the 36 ports was expressed relative to static pressure (N m^{-2}) at a tunnel wall port positioned perpendicular to flow. Data were collected while the model was positioned at 2° intervals from angles of attack of –30 to +30°; for each of the 31 angles considered, data were acquired at 100 Hz for 10 s using LabVIEW software (National Instruments, Inc.). Wind tunnel speed was set according to the Reynolds number considered in water tunnel trials.

Pressure coefficients (C_p) were calculated by dividing the pressure difference above (N m^{-2}) by dynamic pressure ($\rho U^2/2$; where ρ = air density (kg m^{-3}) and U is wind speed (m^2 s^{-1})) determined using a Pitot tube.

Force Measurements

The smooth trunkfish model used in DPIV experiments also was used in force measurement experiments. The model with attached rod was mounted to a sting in a water tunnel with a test section 61 x 45.7 x 244 cm in dimension. Force measurements were collected using three Interface 5 lb strain gauge load cells (Interface, Inc. Scottsdale, AZ) (two load cells measured forces normal to flow [lift], one load cell measured forces parallel to flow [drag]) connected to an in-house force balance (Lisoski, 1993). Output from the load cells was amplified using three Interface SGA amplifiers/conditioners and was recorded using a Dash 8 Series data recorder (Astro-Med, Inc.). Data were collected at 200 Hz for 10 s for each angle considered. As was the case for pressure experiments, force data were collected every 2° from angles of attack of –30 to +30°. Flow speed during trials was identical to that considered in DPIV experiments (2.5 body length s^{-1} (42.5 cm s^{-1})). Coefficients of drag (C_D) and lift (C_L) were calculated using steady-state equations ($C_D = 2*D/(\rho*A_f*U^2)$ or $C_L = 2*L/(\rho*A_p*U^2)$, where D is total drag (N), L is total lift (N), ρ is water density (kg m^{-3}), A_f is maximum frontal area (m^2) and A_p is planform surface area (m^2), and U is water tunnel speed (m s^{-1})).

Results

The development of vorticity along the carapace of a smooth trunkfish positioned at an angle of attack of +10° is depicted in Fig. 3. Vorticity began to develop around the ventro-lateral keels just posterior to the snout at a longitudinal location corresponding to the eye ridge. Peak vorticity and circulation increased posteriorly as the keels became progressively sharper

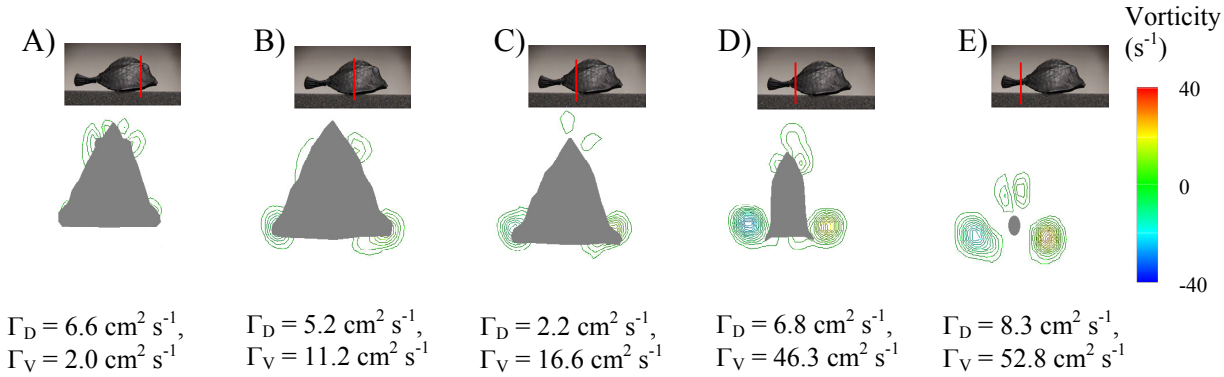

Fig. 3. Vorticity at various transverse planes along the carapace of a smooth trunkfish model positioned at an angle of attack of +10°. The locations considered are: A) eye ridge, B) maximum girth, C) midpoint between maximum girth and posterior edge of carapace, D) posterior edge of carapace, and E) caudal peduncle. Orange and yellow colors depict counterclockwise vorticity, while blues denote clockwise vorticity. Circulation values for a mean dorsal (Γ_D) and mean ventral (Γ_V) vortex are depicted underneath the figures.

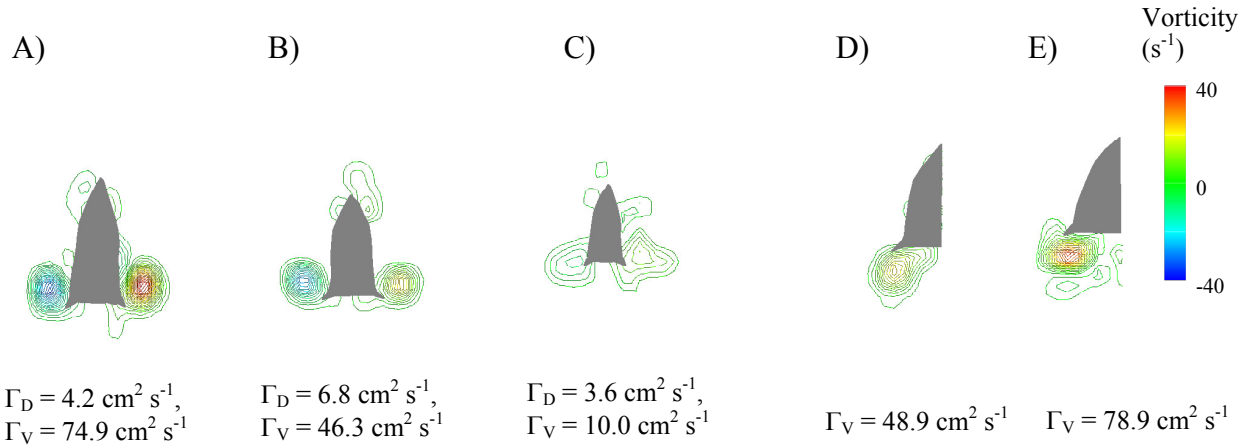

Fig. 4. Vorticity around the posterior edge of the carapace of a smooth trunkfish model positioned at angles of attack of A) +20°, B) +10°, C) 0°, D) –10°, and E) -20°. Circulation values for a mean dorsal (Γ_D) and mean ventral (Γ_V) vortex are depicted underneath the figures. Only half of the models are depicted for negative angles of attack because the other half of the model was shaded from laser light.

until two well-developed counter-rotating vorticies formed at the posterior edge of the carapace. These vortices left the body at the caudal peduncle. Some attached dorsal vorticity also formed along the body, especially around the eye ridge, where circulation was actually stronger dorsally than ventrally. Peak dorsal vorticity and dorsal circulation did not grow steadily along the body, as was the case in ventral regions, and did not reach the magnitudes observed in ventral areas.

Peak vorticity and circulation of carapace-induced vortices were lowest at an angle of attack of 0° (Fig. 4). As the angle of attack deviated further from 0°, either in the positive or negative direction, peak vorticity and circulation intensified (Fig. 4). At positive angles of attack, strong vortices consistently formed above the ventro-lateral keels within concave channels, while attached regions of vorticity with lower peak vorticity and circulation developed either above or beside the dorsal keel. At negative angles of attack, vortices formed below the ventro-lateral keels, and generally little/no vorticity developed along the dorsal keel. Irrespective of angle of attack, peak ventral vorticity and circulation (of attached vortices) were always greatest at the posterior edge of the carapace, which is posterior to the center of mass.

There was a correlation between regions of attached vorticity observed in DPIV experiments and regions of low pressure detected in pressure experiments. Along the eye ridge dorso-ventral transect, low pressure was observed at pressure port B4 at a 10° angle of attack, which is also where attached vorticity was detected in DPIV experiments (Fig. 5). At a location just above the ventral keel (pressure port B1), attached vorticity was observed in DPIV experiments. In pressure experiments, pressure dropped at B1 relative to neighboring port B2 along a dorso-ventral transect (Fig. 5). Along the maximum girth dorso-ventral transect, attached vorticity formed laterally and above the ventro-lateral keels, which correspond to pressure ports B7 and B11, respectively. Pressure dropped at B7 relative to its dorsal neighbor B6, and pressure was very low at B11. Along a transect halfway between the point of maximum girth and the posterior edge of the carapace, both attached vorticity and low pressure were observed just above the ventro-lateral keel (pressure port B12). Finally, at the posterior edge of the carapace, a strong vortex was observed above the ventro-lateral keel; at this location (B20 on pressure models) low pressure relative to other points along a dorso-ventral transect was observed (Fig. 5).

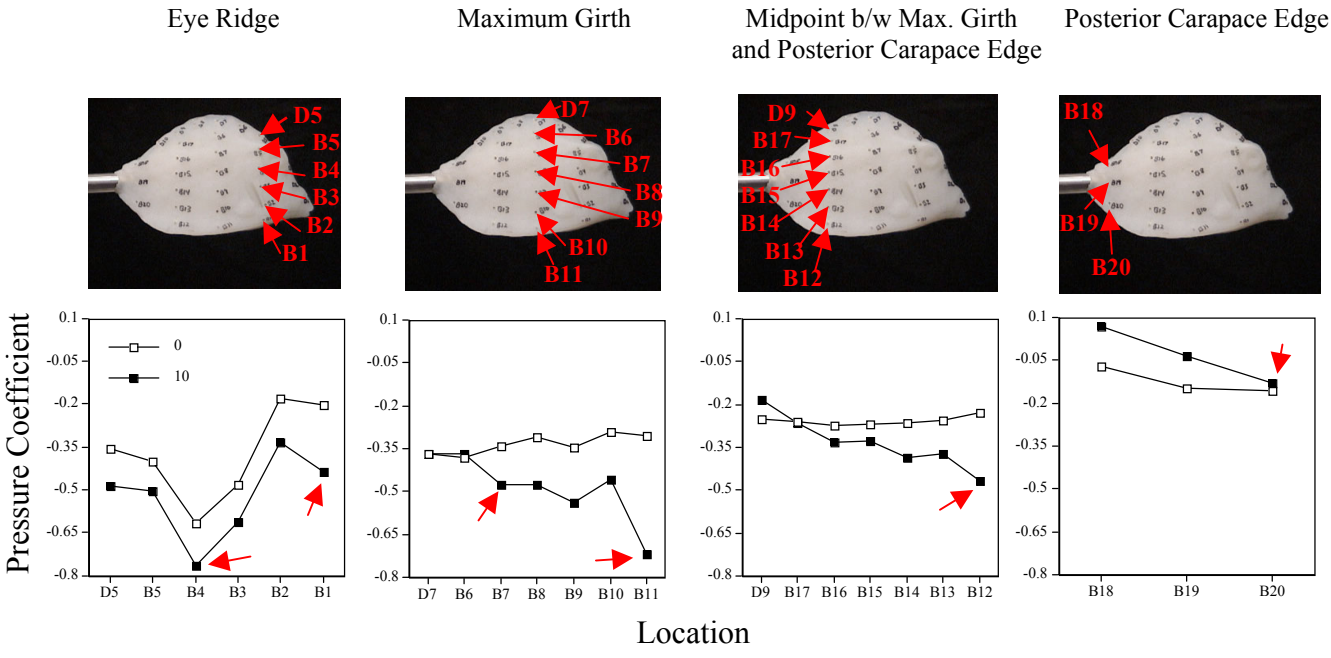

Fig. 5. Pressure coefficients at various dorso-ventral transects along a smooth trunkfish model positioned at angles of attack of 0° (open squares) and +10° (shaded squares). The pressure ports considered in each graph are highlighted in the images above. Red arrows in pressure graphs highlight regions where vorticity was detected in DPIV experiments

Although peak vorticity and circulation associated with the ventral keels increased consistently along the carapace from eye ridge to the posterior edge of the carapace, pressure values did not decrease consistently along the carapace (Fig. 6). Instead ventro-lateral pressure decreased from the snout to the point of maximum girth (B11), but then increased posteriorly thereafter. Along a dorso-lateral transect where regions of attached vorticity were observed, pressure was lowest above and behind the eye ridge (D4, B5), but then increased longitudinally along the body, even at B18, where circulation of dorsal vorticity was similar to that measured for eye ridge vorticity (Fig. 6). The values in Fig. 6 are upward directed torque measurements (N m) about the center of mass for 1 cm^2 regions. Although pressure is lowest at B11, it has effectively no impact on pitch correction because it is dorso-ventrally aligned with the center of mass.

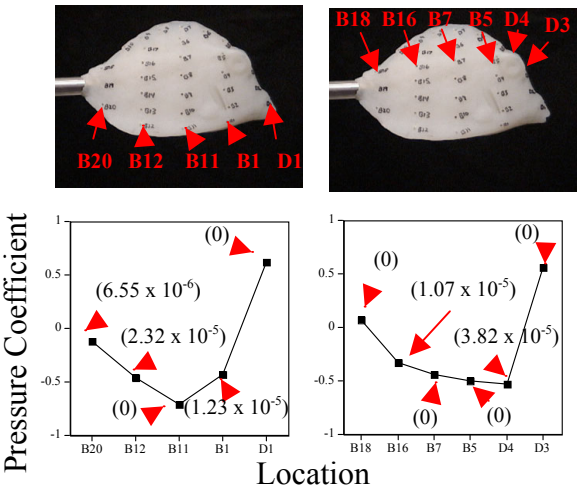

Fig. 6. Pressure coefficients at two antero-posterior transects along a smooth trunkfish model positioned at a +10° angle of attack. The locations of the pressure ports are highlighted in the images above. Values in the graphs are upward directed torque (N m) about the center of mass at a 1 cm^2 region.

B1, B12, and B20 have a larger impact on pitching because they are anterior or posterior to the center of mass. Along a dorso-lateral transect, B7 has little impact on pitching since it too is dorso-ventrally aligned with the center of mass, and no upward directed torque is produced at B5 because it is parallel to the dorso-ventral axis of the fish.

Lift and drag coefficients are depicted in Fig. 7. Minimum drag occurred at an angle of attack of –2°, indicating that there is a difference between geometric and dynamic zero. No stall occurred at angles of attack $\pm$ 30°, and overall coefficients were similar to those observed by Schlichting and Trunkenbrodt (1969) for a delta wing of similar aspect ratio.

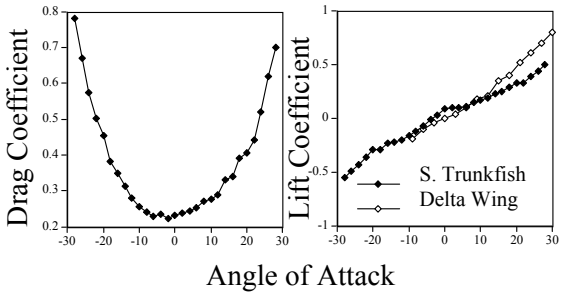

Fig. 7. Drag coefficients for a smooth trunkfish model positioned at angles of attack $\pm$ 30°, and lift coefficients for a smooth trunkfish model and a delta wing with a 0.83 aspect ratio (Schlichting and Truckenbrodt, 1969). Smooth trunkfish coefficients are depicted as shaded diamonds, while delta wing coefficients are depicted as open diamonds.

Discussion

The results of this study indicate that the ventro-lateral keels of the smooth trunkfish are useful for vortex generation. As angles of attack deviate from 0° in the positive direction, stronger peak vorticity and circulation develop along lateral concavities above ventro-lateral keels, reaching maximum strength at postero-lateral regions of the carapace. As angles of attack deviate from 0° in the negative direction, stronger peak vorticity and circulation develop along ventral concavities below ventro-lateral keels, reaching maximum strength at postero-ventral regions of the carapace. The effects of these vortices on the body are strongly influenced by the complex geometry of the carapace near the developing vortex. The strongest peak vorticity and circulation generally develop posterior to the center of mass and above (positive angles of attack) or below (negative angles of attack) ventral keels that extend laterally at an angle of 30-40° relative to a horizontal axis when viewed in cross-section. Consequently, suction derived from the presence of a vortex above or below the ventral keels will act largely upward and posterior to the center of mass at positive angles of attack and downward and posterior to the center of mass at negative angles of attack. The ventral keels thus are effectively generating self-correcting forces for pitching motions; the degree of self-correction is proportional to the degree to which the fish is perturbed from a horizontal swimming trajectory.

While DPIV provides a picture of what is happening globally around the carapace, pressure

measurements provide useful information on flow conditions at the carapace surface. Pressure measurements along dorso-ventral transects similar to those considered in DPIV studies correlate well with DPIV results; in regions where attached vorticity was observed, low pressure also was detected. This was largely the case in dorsal regions as well, with attached vorticity around the eye ridge correlating well with low-pressure measurements. However, when viewed along antero-posterior transects there was less concordance. Along a ventro-lateral keel, pressure was lowest at the point of maximum girth and did not continue to decrease along the body as expected based on DPIV results. This may be because although peak vorticity and circulation increase posteriorly along the body, the vortex core actually migrates away from the body and has less impact on the actual surface of the carapace. The movement of the vortex core away from the body may be seen in Fig. 3.

The geometry of the carapace and location of the center of mass have significant impacts on the magnitude of pitch correction. As presented in the results, pressure at a 10° angle of attack was low at B11, a location just above the ventro-lateral keel close to the point of maximum girth, but pressure at this location has little effect on pitching since it is dorso-ventrally aligned with the center of mass. Pressure at B1 and B12, which are in front and behind the center of mass along the dorso-ventral keel, respectively, have a larger impact on pitching motions, producing far greater upward directed torque (about the center of mass) at positive angles of attack. At D4, which is located above the eye ridge in an area that is close to being horizontal relative to free-stream flow (< 15°), considerable upward directed forces are generated; conversely at B5, which is also located in a low pressure region of the eye ridge, effectively no upward directed forces are produced because it is oriented parallel to the dorso-ventral axis of the fish. Interestingly, the eye ridge generates an optimal pressure distribution around the eye, i.e., ambient pressure is produced. This is advantageous since the eye (and most importantly the lens) will not be pushed in or pulled out as flow moves along the body. Pressure measurements along the carapace, knowledge of the location of the center of mass, and detailed morphological information of the carapace surface (obtained from CT scans) allow for the precise calculation of self-correcting forces generated by vortex formation. In present studies, additional holes at the posterior edge of the carapace are being sampled to provide a more detailed pressure distribution around the body, which ultimately will be used to accurately compute the magnitude of self-correcting forces.

Based on DPIV and pressure results, vortices develop around the carapace, most prominently in regions adjacent to ventro-lateral keels, and produce both overall lift and self-correcting lift for pitching. The force measurements provide further evidence of vortex formation. Lift coefficients in smooth trunkfish resemble those of delta wings, devices that generate lift through vortex generation and not bound circulation like conventional aircraft wings. The flow field over a delta wing, where a coiled vortex sheet forms and grows along the wing, is such that the resultant pressure distribution produces a large nose-down (negative) pitching moment about the apex, especially at high angles of attack (Bertin and Smith, 1989). As discussed above, a similar pitching moment develops in smooth trunkfish as a result of vortex growth along the body at positive angles of attack, and this is useful for pitch correction. Taking the delta wing analogy one step further, structures are often positioned near the leading edge of delta wings (e.g., apex flaps/fences) to interact with the developing coiled vortex sheet and improve maneuverability through vortex bursting (Wahls et al., 1986). The pectoral fins of the smooth trunkfish, which are located near the leading edge of vortex formation, may serve a similar function.

The results of the three independent, but complementary experimental approaches, indicate that the ventro-lateral keels of the smooth trunkfish act as vortex generators, producing overall lift and self-correcting forces for pitching. The ventral keels thus help stabilize the smooth boxfish as it swims in highly turbulent waters, and are of interest to designers of biomimetic AUVs. The eye ridges produce vorticity as well, which may be used to optimize visual systems or possibly the efficacy of fins. Now that we have a comprehensive understanding of the dynamic properties of the body, we can separate out the contributions of the body from those of the fins in future studies and examine the complex interaction between fin movements and body vortex formation. This work, which will be performed using 3D defocusing digital particle image velocimetry (DDPIV) (Pereira et al. 2001), should provide unprecedented information on the stability and maneuverability of rigid-body multi-propulsor swimmers.

Acknowledgments

We thank R.M. Alexander and J. Hove for valuable input, M. McNitt-Gray, J. Carnahan, B. Valiferdowsi, and P. Masson for aid during model construction, D. Lauritzen and S. Bartol for assistance during data collection, and D. Dabiri, L. Zuhal, and D. Jeon for technical assistance. Financial support of the Office of Naval Research under contract N00014-96-0607 is gratefully acknowledged.

References

Bertin, J.J. and M.L. Smith. 1989. *Aerodynamics for Engineers*, 2nd edition. Englewood Cliffs: Prentice Hall.

Gordon, M.S., J.R. Hove, P.W. Webb, and D. Weihs. 2000. Boxfishes as unusually well-controlled autonomous underwater vehicles. *Phys. Biochem. Zool*. 73 (6): 663-671.

Hove, J.R., L.M. O'Bryan, M.S. Gordon, P.W. Webb, and D. Weihs. Boxfishes (Teleostei: Ostraciidae) as a model system for fishes swimming with many fins: kinematics. *J. Exp. Biol*. 204: 1459-1471.

Liposki, D. 1993. *Nominally 2-dimensional flow about a normal flat plate*. Ph.D. dissertation, California Institute of Technology.

Lorenson, W.E. and H.E. Cline. 1987. Marching cubes: a high resolution 3D surface construction algorithm. *ACM Comp. Graph*. 21: 163-169.

Nelson, J.S. 1994. *Fishes of the World*, 3rd Ed. New York: John Wiley and Sons.

Pereira, R., M. Gharib, D. Dabiri, and D. Modarress. 2000. Defocusing DPIV: a 3-component 3-D DPIV measurement technique. Application to bubbly flows. *Exp. Fluids* 29: S078-S084.

Raffel, M., C.E. Willert, and J. Kompenhans. 1998. *Particle Image Velocimetry: A Practical Guide*. Berlin: Springer-Verlag.

Schlichting, H., and E. Truckenbrodt. 1969. *Aerodynamik des Flugzeuges*, Vol. 2, Ch. 7, Berlin: Springer-Verlag.

Wahls, R.A., R.J. Vess, and C.A. Moskovitz. 1986. Experimental investigation of apex fence flaps on delta wings. *J. Aircraft* 23: 789-797.

Willert, C.E. and M. Gharib. 1991. Digital particle image velocimetry. *Exp. Fluids*. 10: 181-193.